Accuracy assessment for mapping glacier flow velocity and detecting flow dynamics from ASTER satellite imagery: Tasman Glacier, New Zealand

T.A.N. Redpath[a], P. Sirguey[b,*], S.J. Fitzsimons[a], A. Kääb[c]

[a]*Department of Geography, University of Otago, P.O. Box 56 Dunedin, New Zealand*
[b]*School of Surveying, University of Otago, P.O. Box 56 Dunedin, New Zealand*
[c]*Department of Geosciences, University of Oslo, P.O. Box 1047 Blindern, Oslo, Norway*

Abstract

Image matching via correlation of remotely sensed imagery is an increasingly popular technique for measuring glacier flow because it can provide spatially distributed measurements while mitigating many of the challenges accompanying *in situ* measurements of glacier velocity. Despite the increasing use of such techniques, and the requirement for well understood uncertainties where analysis of temporal variability is sought, studies that incorporate an assessment of accuracy based on *in situ* data remain rare. This study presents a rigorous methodology to quantify the uncertainties that apply to glacier flow velocities derived from optical satellite imagery. This method is applied on three successive ASTER images of Tasman Glacier, New Zealand. Evaluation of the quality of co-registration between image pair constituents allows unique uncertainties to be calculated for individual velocity measurements. These uncertainties have magnitudes that correspond to sub-pixel co-registration errors and account for anisotropic co-registration variance. Compared to estimated velocities, uncertainties on the order of 2–30% are achieved. Flow-fields for the 2009–2010 and 2010–2011 periods were derived using various spectral bands and validated with *in situ* data obtained by GPS survey over a nearly coincident period. This revealed the importance of considering the spectral characteristics of the target surface when selecting bands for image correlation, while validation demonstrated the success of the implemented methodology. Uncertainties derived for the flow-fields permitted statistical significance of velocity change between measurement periods to be assessed. Significant velocity changes, observed across the glacier surface, suggest that the Tasman Glacier behaves in a more dynamic way than previously recognised, highlighting the advantages of the methodology described here.

Keywords:
Image matching, Optical Imagery, Glacier, ASTER, Surface displacement, Accuracy, Tasman Glacier

1. Introduction

Since the earliest examples of glacier flow measurement from satellite imagery (e.g., Lucchitta & Ferguson, 1986), increases in the availability and quality of remotely sensed datasets have allowed substantial progress to be made in glaciological research (Scambos et al., 1992; Berthier et al., 2003; Kääb, 2005b). Remote sensing techniques have the benefit of providing spatially distributed observations, while mitigating many of the logistical problems associated with *in situ* measurements of glacier flow velocity (Hubbard & Glasser, 2005; Scherler et al., 2008). Since the analogue approach used by Lucchitta & Ferguson (1986), digital approaches, including computer pre-processing of imagery, have substantially improved remote sensing methodologies for glaciological studies, and the accuracy of the measurements made. Automatic image matching techniques, developed using cross co-variance correlation functions implemented in the spatial or frequency domains, form the basis of most currently used packages for measuring displacements of features in optical imagery (e.g., Scambos et al., 1992; Kääb & Vollmer, 2000; Berthier et al., 2005; Leprince et al., 2007; Heid & Kääb, 2012).

The measurement of displacements by image matching is reliant on the co-registration between image pair constituents (Scherler et al., 2008), as well as the removal of geometric distortions in each image by means of precise ortho-rectification. A level of spatial uncertainty always accompanies the ortho-rectification process, in turn governing the accuracy with which motion on the target surface may be measured (Kääb, 2005b,a; Leprince et al., 2007; Scherler et al., 2008). In the context of ortho-rectification of satellite imagery, a maximum average Root Mean Square (RMS) error of ±1 pixel is typically sought across the image. When considering an image pair, the resulting uncertainty in co-registration compounds that inherent to the cross-correlation used for image matching (e.g., Berthier et al., 2003).

Thorough quantification of the uncertainties accompanying image pair co-registration is still not widespread. Such uncertainties, represented by an RMS error computed from a set of stable control points (CPs), are a combination of systematic (i.e., an apparent bias, or shift between constituents of an

*Corresponding Author
Email addresses: redpath.todd@gmail.com (T.A.N. Redpath), pascal.sirguey@otago.ac.nz (P. Sirguey), sjf@geography.otago.ac.nz (S.J. Fitzsimons), kaeaeb@geo.uio.no (A. Kääb)

image pair) and random error. The former can be readily corrected, while the latter may be statistically modelled. Since co-registration quality is a primary control on the accuracy of velocity measurements made by image matching, it is necessary to improve understanding and quantification of co-registration quality and uncertainty.

This paper presents a methodology developed for monitoring flow dynamics on a glacier surface, using image matching (cross-correlation) techniques implemented in the spatial domain. Specifically, a straight-forward, yet robust means to reliably detect temporal variability in glacier flow is presented. Change detection is facilitated via rigorous quantification of the uncertainty affecting the accuracy of displacements measured on the glacier surface. Additionally, flow velocity measurement from image matching are derived using various spectral bands and validated with *in situ* measurements of glacier flow, obtained by GPS survey. This highlights the importance of band selection for image matching, for instance due to the significant influence of local lithology in case of debris covers. Finally, this method is applied to derive the surface flow-field of the Tasman Glacier, New Zealand, for two recent image pairs (2009–2010, 2010–2011) in order to detect areas of significant velocity change.

2. Study area and data

2.1. Study area

The Tasman Glacier, New Zealand's longest and largest (Chinn, 2001), is located in Aoraki/Mt Cook National Park in the Southern Alps of the South Island (Figure 1). With a current length of approximately 25 km, it flows south from its accumulation area located high on the main divide of the Southern Alps. Surrounded by New Zealand's highest peaks, including Aoraki/Mt Cook (3,754 m), numerous tributary glaciers contribute to the flow regime. The glacier is constrained by the Mt Cook Range and the main divide of the Southern Alps to the West, and the Liebig and Malte Brun ranges to the East. The area is tectonically active, with the Alpine Fault located less than 30 km to the west of the main axial ridge of the Southern Alps (Cox & Barrell, 2007).

Local geology is dominated by Triassic to Permian age Torlesse Greywacke, a low grade metamorphic rock of sandstone origin (Cox & Barrell, 2007). Metamorphism increases with proximity to the Alpine Fault, with Schists found west of the Main Divide (Cox & Barrell, 2007). Substantially weakened by rapid tectonic uplift (up to 10 mm a^{-1}), and subsequent faulting and folding, the Torlesse Greywacke is prone to mass movement on steep slopes (Allen et al., 2009; Cox & Barrell, 2007). Frequent rock avalanches help sustain a relatively thick debris cover on most valley glaciers within the Southern Alps, including the Tasman Glacier. The Tasman Glacier terminates in the proglacial Tasman Lake. Recent rapid retreat of the glacier has seen Tasman Lake grow from a group of small thermokarst lakes to a substantial water body (Kirkbride, 1993; Strong, 2008).

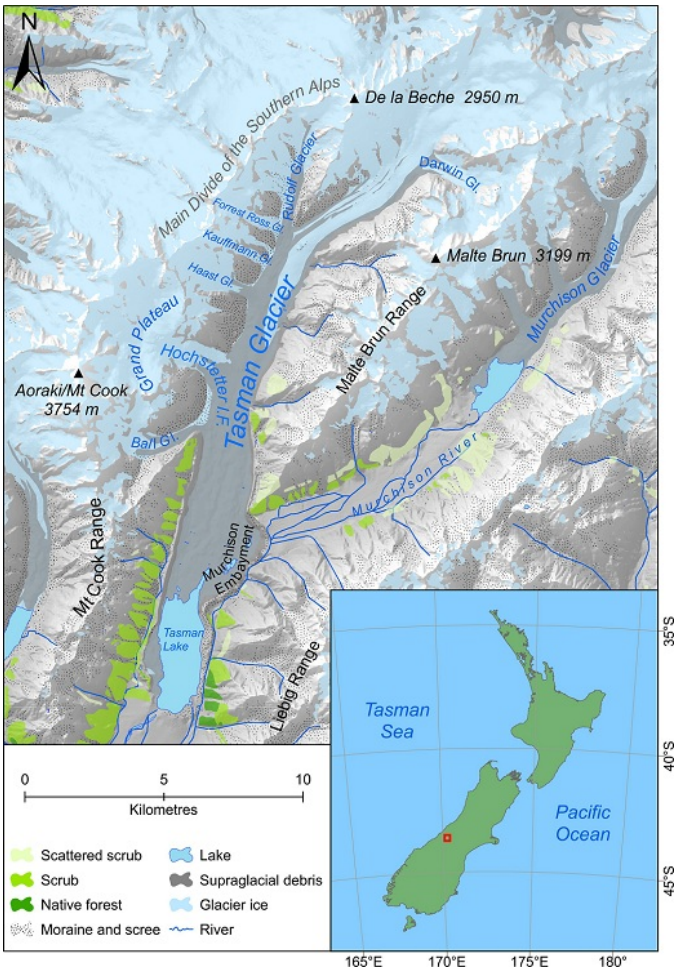

Figure 1: Map of the Aoraki/Mt Cook area, showing the location of the Tasman Glacier in the central Southern Alps of New Zealand. Topographic data from the LINZ NZTopo Database.

2.2. Flow velocity of the Tasman Glacier

Several ground-based studies of surface motion have been carried out on the Tasman Glacier, providing a range of measurements. Brodrick (1891, 1894) measured velocities as high as 167 m a^{-1} near the Ball Glacier confluence during the Austral summer of 1890/1891. Later, Anderton (1975) reported annually averaged surface velocities of up to 244 m a^{-1} on the upper glacier, below Malte Brun. Kirkbride (1995) later measured average surface velocities of up to 98 m a^{-1} South of Ball Glacier and mapped velocities in the lower Tasman, South of the Murchison Embayment (see Figure 1), from the displacement of boulders visible in aerial photos acquired in 1957, 1971, and 1986. This author concluded that surface velocities generally decreased during this period by an amount that depends on the distance to the terminus. The spatial variability of the surface velocity, however, compounded with the expected temporal variability, could hardly be resolved by the sparse punctual measurements in space and time.

Addressing the spatial variability of the surface velocity was enabled by the use of repeated satellite imaging. The surface motion of the Tasman Glacier was thus estimated by Kääb

(2002, 2005b) who used the image correlation software CIAS to derive flow fields from two successive pairs of ASTER images. The spatial distribution of velocity differences led Kääb (2005b, pg. 132-133) to conclude that a significant increase of surface velocity occurred over the period 2000-2002. In addition, the very low velocity observed at the Hochstetter confluence was interpreted as a possible de-coupling between the upper Tasman and Hochstetter glaciers.

Quincey & Glasser (2009) used the COSI-Corr image matching software (Leprince et al., 2007) to derive flow fields from ASTER images for periods in January–December 2002 and January 2006–December 2007. These measurements are considered to be disconnected on the basis that some time has lapsed between each of the two measurement periods. Although their findings largely echoed that of Kääb (2002) in terms of the spatial structure of the flow, Quincey & Glasser (2009) were unable to draw conclusions about the temporal variability of the flow-field of the Tasman Glacier over this period. Recently, Herman et al. (2011) derived flow velocity fields for the Tasman Glacier from two pairs of ASTER images acquired only 16 days apart, on two disconnected periods in 2002 and 2006. Despite the large errors observed for velocity less than 182 m a^{-1} (most of the flow rate of Tasman Glacier), Herman et al. (2011) inferred no change in velocity and described Tasman Glacier as a "slow-response glacier".

The contradicting results of Kääb (2005b, pg. 132-133), Quincey & Glasser (2009), and Herman et al. (2011) highlight the need to assess the reliability of glacier flow maps via ground validation. Furthermore, a rigorous quantifification of the uncertainties associated with the surface velocity of Tasman Glacier is desirable to improve the reliability of conclusions regarding ice flow dynamics.

2.3. *Field data*

Three GPS survey campaigns were carried out. GPS survey data provided ground information for spectral band performance assessment, and subsequently allowed the overall accuracy of the flow-fields derived from ASTER imagery to be assessed. Ten survey markers were installed between April 13–16, 2009 around the Hochstetter Confluence (Figure 2). They were installed on large rocks on the debris covered region of the glacier surface; their position was surveyed using a Leica SR20 GPS receiver in static mode. The second campaign carried out between April 6 – 10, 2010 was coincident with the acquisition of the ASTER image (April 9, 2010). Eight of the 10 markers installed in 2009 were found and their positions re-surveyed using a Trimble R8 GPS receiver, executing a fast static survey. Eight additional markers were installed to increase the spatial coverage of the network (Figure 2). All 16 markers were re-surveyed on April 27–29, 2011. This yielded a total of 24 velocity measurements over the two-year period.

Technical difficulties limited the occupation times at each marker during the first survey, while the occupation time at each marker exceeded 10 minutes during the two following surveys. For all surveys the Position Dilution of Precision (PDOP) never exceeded 4.5 and was generally less than 2. GPS data were

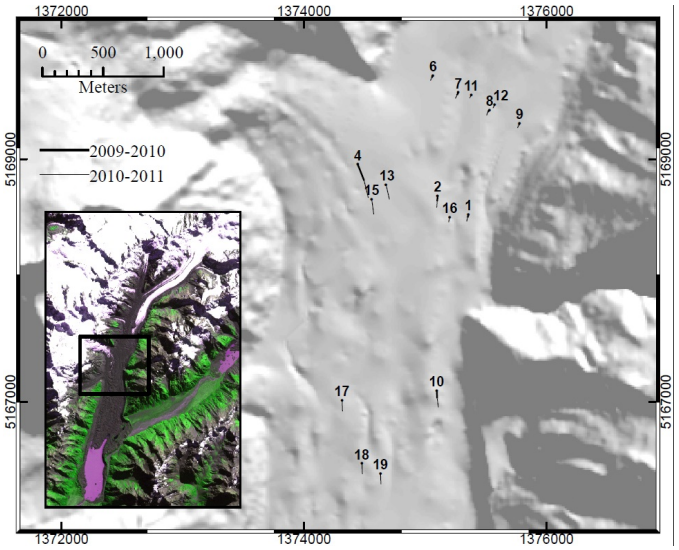

Figure 2: Location of markers near the Hochstetter confluence. The vectors show the displacements measured over the 2009-2010 and 2010-2011 periods.

differentially corrected afterwards using data from the nearest Land Information New Zealand (LINZ) PositioNZ Network continuous GPS receiver at Mt John observatory. On each survey, the consistency of the positional error was cross-assessed by repeatedly surveying a nearby level two mark of the national geodetic network (also maintained by LINZ) at the commencement and conclusion of each field campaign.

2.4. *Satellite imagery*

Displacement measurements on the glacier surface were made by image matching using the Correlation Image Analysis Software (CIAS) (Kääb & Vollmer, 2000; Kääb, 2005b). Three ASTER images, whose time of acquisition was close to that of the ground surveys (Table 1), provided two successive image pairs supporting two connected measurement intervals of 416 and 328 days, respectively (i.e., the time separating acquisition of image pair constituents). CIAS was used to estimate flow velocities, as well as to quantify the uncertainties associated with the velocity estimates.

The images were ortho-rectified with PCI Geomatica v10 using the ASTER satellite orbital model (Toutin, 2004) when the pointing angle was nadir. This allows most distortions, including lower-order components of platform attitude variations, to be accounted for. Alternatively, better results were obtained by using the rational function model when the sensor pointed off-nadir, at the expense of the need for more Ground Control Points (GCP). Elevation information was provided by the nationwide 15 m resolution Digital Elevation Model (DEM) NZSoSDEMv1 (Columbus et al., 2011). For each image, a set of Check Points (CP) was used to assess the quality of each geometric correction as shown in Table 1. GCPs and CPs for image ortho-rectification were primarily provided by GPS surveys conducted in and around the area, as described in Gjermundsen et al. (2011) and were manually located in the images. Additional points were obtained from the national topographic

Table 1: List of ASTER images. Ortho-rectification parameters include the number (no.) of ground control points (GCPs) and control points (CPs) used, and the RMS error in x and y directions (in pixel), for each image. * Indicates that a mosaic was made with both granules.

		GCPs			CPs		
Acquisition date	Look angle	no.	RMS x	RMS y	no.	RMS x	RMS x
2009-Feb-17 22:38:29	-0.019	28	0.58	0.52	15	0.75	0.55
2010-Apr-09 22:37:37	-0.017	27	0.33	0.25	14	0.58	0.36
2011-Mar-02 22:43:20*	8.586	53	0.28	0.37	20	0.63	0.52
2011-Mar-02 22:43:29*	8.586	94	0.32	0.34	31	0.61	0.54

database (NZTopo, 1 : 50,000 scale) when needed depending on the coverage of each ASTER image and the ortho-rectification model used.

All images were considered to be independently ortho-rectified because different combinations of GCPs and CPs were identified in each image separately and no image provided a basis of co-registration for the others. This process does not readily ensure a perfect co-registration of image pairs and may affect the measurements derived from image matching. Therefore, a quantification of the co-registration was required as explained in Section 3.5.

3. Method

3.1. Reference displacements measured from GPS surveys

The total displacement of a marker was calculated from coordinates projected in terms of the New Zealand Transverse Mercator (NZTM) grid as

$$l = \sqrt{\Delta x^2 + \Delta y^2}, \tag{1}$$

where Δx and Δy are the Easting and Northing displacements, respectively. The displacements were then converted to reference velocities (m a^{-1}) based on the time difference between both surveys (i.e., 358 and 360 days). Post-processing of GPS survey data yielded error ellipses for each point characterized by different standard deviation in the x and y directions, namely σ_x and σ_y. The uncertainty associated with the displacement vectors and, subsequently, velocities, was calculated in accordance with error propagation theory (Taylor, 1997). Differentiating Eq. (1) yields

$$dl = \frac{\partial l}{\partial \Delta x} d\Delta x + \frac{\partial l}{\partial \Delta y} d\Delta y. \tag{2}$$

Since $\frac{\partial l}{\partial \Delta x} = \frac{\Delta x}{l}$, and similarly $\frac{\partial l}{\partial \Delta y} = \frac{\Delta y}{l}$, it comes that

$$dl = \frac{\Delta x}{l} d\Delta x + \frac{\Delta y}{l} d\Delta y. \tag{3}$$

This allows the variance associated with l to be estimated by

$$\mathrm{Var}\left[l\right] = \left(\frac{\Delta x}{l}\right)^2 \mathrm{Var}\left[\Delta x\right] + \left(\frac{\Delta y}{l}\right)^2 \mathrm{Var}\left[\Delta y\right]. \tag{4}$$

In turn, a rigorous estimate of the standard deviation of l is provided by

$$\sigma_l = \sqrt{\left(\frac{\Delta x}{l}\right)^2 \left(\sigma_{x_1}^2 + \sigma_{x_2}^2\right) + \left(\frac{\Delta y}{l}\right)^2 \left(\sigma_{y_1}^2 + \sigma_{y_2}^2\right)}, \tag{5}$$

where the subscripts 1 and 2 indicate the times of survey. The uncertainties were finally converted to m a^{-1}.

3.2. Band selection for image matching

Image matching techniques operate on a pair of single channel images. Recent studies have shown that the performance of image matching can be improved by selecting an appropriate band and by using image processing techniques, such as a high-pass filter to enhance features prior to detection (Ahn & Howat, 2011; Heid & Kääb, 2012). Nevertheless, previous glaciological studies have typically used the near infrared (NIR) ASTER band 3 (see Quincey & Glasser, 2009; Herman et al., 2011), seemingly relying on the performance of ASTER band 3 over ice and snow, despite the fact that most of the area of interest is, in the case of the Tasman Glacier, debris covered.

This study first compared the performance of CIAS based on different channels derived from the ortho-rectified images at the original pixel size (i.e., 15 m). ASTER bands 1, 2, and 3 were tested, as well as single channel images created from linear combinations of the above which could exhibit better contrast and facilitate image matching. First, an intensity band (the results of an Intensity-Hue-Saturation transformation and comparable to a panchromatic channel) was formed from the ASTER Visible and Near Infrared (VNIR) bands. Second, a principal component analysis was computed with the VNIR bands. The channel with maximum variance (PC_1) was retained for image matching, having been recognized as enhancing surface topography and texture (Adams & Gillespie, 2006, pg. 83). Finally, ASTER band 3 was convolved with a high-pass (HP) filter to enhance the prominence of ground features which could facilitate their detection. This process was repeated for both successive pairs of images (i.e., 2009-2010 and 2010-2011).

The 24 velocities measurements obtained from GPS surveys were compared to estimates obtained from CIAS for each type of image. The success rate (SR) was quantified as the percentage of correct matches following a visual assessment. Additionally, the performance of each channel was measured by the coefficient of determination (R^2) associated with the linear regression over all measurements, as well as the Root Mean Square Error (RMSE) between the estimated and measured velocities

at each location. Finally, the mean and standard error of the correlation coefficients returned by CIAS were computed as it provides indication of the overall quality of the matches (i.e. $\bar{\rho}$ and σ_ρ).

3.3. Image resampling

In the context of satellite image matching, displacements can be measured at a sub-pixel level by relying on resampled images (Scherler et al., 2008; Debella-Gilo & Kääb, 2011). Resampling to one tenth of the original pixel size (i.e., 1.5 m) was conducted to derive more precise velocities, as well as to assess more precisely the co-registration of image pairs. Resampling was carried out concurrently to the ortho-rectification process using a sixteen point cardinal sine function (Dodgson, 1992; Berthier et al., 2005). Resampling concurrently to ortho-rectifiation mitigated the risk of introducing additional distortion to the ortho-images.

3.4. Derivation of flow-fields

CIAS relies on a two dimensional cross-correlation function, implemented in the spatial domain, and operating on image grey values (Kääb, 2005b, Section 4.4). Image matching on the Tasman Glacier relied on the extensive debris cover of the lower part of the glacier providing a number of heterogeneous and contrasting targets. Crevasses were not relied on for image matching on the Tasman Glacier because crevasses are constrained by underlying topography affecting the distribution of strain within the ice mass (Paterson, 1994). Subsequently, they are not a well preserved feature that is conveyed by the flow of temperate valley glaciers, rendering them unreliable as targets for measuring surface velocity over measurement intervals of the length used here.

Velocity across the surface of the Tasman Glacier was derived based on a 150 m grid constrained by glacier outlines. In CIAS a search window size of 600 × 600 pixels (in the ten-fold resampled image) allowed for movement of up to 450 m positively or negatively in the x and y directions, accommodating the maximum movement expected for this glacier. A reference window of 105 pixels was found to be suitable to maximise the cross-correlation within an acceptable computing time. Data filtering and cleaning was required to eliminate spurious mis-matches. All measurements with a correlation coefficient less than 0.6 were removed from the data set. In addition, directional filtering was used to eliminate northward displacements that were inconsistent with the gradient driven southward flow of the glacier. Remaining displacement vectors were visually assessed for consistency and remaining spurious measurements were removed. The displacements were then converted to velocities based on the time difference between both images. The resulting voids in the flow-field were interpolated using Kriging. This approach was justified by the high spatial auto-correlation exhibited by the datasets as demonstrated by Moran's I values (Moran, 1950) and the empirical semi-variograms shown in Fig. 3. The latter exhibits a significantly increasing variance of velocity as the lag distance between the locations of the measurements increases. This characterization

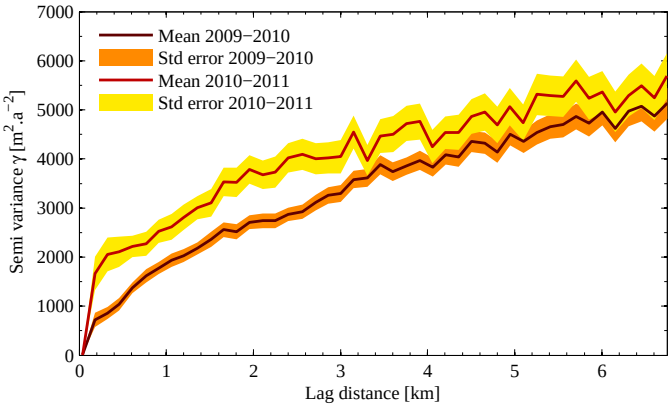

Figure 3: Semi-variogram of the velocity estimates derived from image pairs 2009-2010 and 2010-2011. The variance of velocity increases significantly as the lag distance the locations of the measurements increases. This characterizes the spatial auto-correlation of the field of measurements that justifies the use of Kriging interpolation.

of the spatial auto-correlation provides a suitable geo-statistical context for the Kriging interpolation.

3.5. Uncertainties of the velocity measurements derived by image matching

3.5.1. Theoretical approach

The quality of co-registration between ortho-images is a primary source of uncertainty when deriving flow-fields by image matching. In this study, the co-registration error of an image pair is the result of the ortho-rectification error associated with each ortho-image forming the pair. During the ortho-rectification process, a set of well-chosen and positioned GCPs should ideally provide no bias in the geolocation of each ortho-image, eliminating any rigid translation between ortho-images, and thus resulting in an unbiased co-registration of the image pair (i.e., $\mu_x = \mu_y = 0$). Subsequently, the RMS residual of the positions of the control points (CPs) used to assess the ortho-rectification of each image represent the standard deviation of a Gaussian random error affecting the x and y coordinates of each image pixel equally. Under this assumption, image pair co-registration, although unbiased, is affected by random error of known variance. Consequently, the standard deviation associated with directional displacements Δx and Δy derived from the image pair are identical and satisfy

$$\sigma_c = \sqrt{\sigma_1^2 + \sigma_2^2}, \tag{6}$$

where σ_1 and σ_2 are the standard deviation associated with the imperfect ortho-rectification of each image forming the pair, respectively.

In this context Herman et al. (2011) and Necsoiu et al. (2009) indicate that the displacement $l = \sqrt{\Delta x^2 + \Delta y^2}$ obeys a Rayleigh distribution with mean $\sigma_c \sqrt{\pi/2}$ and standard deviation $\sigma_c \sqrt{(4-\pi)/2}$. The final uncertainty associated with the displacement l arises from the compounded effects of the mean (which results in a positive bias of the displacement estimates) and the standard deviation of the skewed Rayleigh distribution.

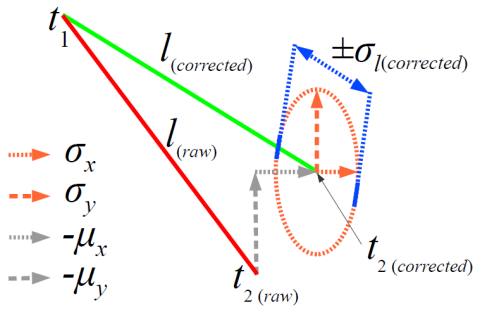

Figure 4: Representation of the correction for bias and derivation of uncertainty for a displacement vector measured via image matching.

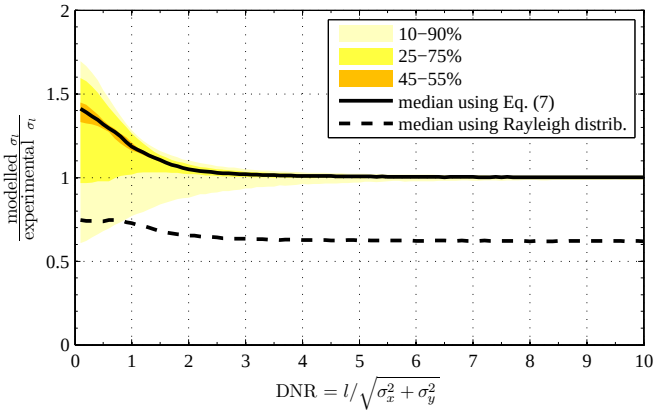

Figure 5: Distribution of the Monte Carlo realizations comparing the modelled and experimental standard deviations associated with displacements affected by random noise as a function of the Displacement to Noise Ratio (DNR). The median and selected percentiles of the set of realizations are shown when using the error propagation theory. Only the median associated with the use of the Rayleigh distribution is shown for clarity.

The Rayleigh distribution, however, supposes non-biased Gaussian noises of equal variance. As such, its use should be limited to displacements that are expected to be null (i.e., $l = 0$). Alternatively, non-null displacements (i.e., $l > 0$) affected by equal directional uncertainty (σ_c) obey a Rice distribution of parameters l and σ_c. This distribution is not trivial and reduces to the Rayleigh distribution only when $l = 0$. As l increases, so does the variance of the Rice distribution, while the mean converges to the expected displacement l. Consequently, reliance on the Rayleigh distribution for derivation of displacement uncertainties, caused Herman et al. (2011) to underestimate uncertainties by up to a factor $\sqrt{(4-\pi)/2}$, depending on the magnitude of the displacement in question.

Furthermore, the assumptions that (i) the co-registration of the image pair is unbiased, and (ii) that standard deviations of the co-registration errors are equal in both the x and y directions, are restrictive and sometimes inappropriate. For example, Necsoiu et al. (2009) and Leprince et al. (2007) reported a substantial anisotropy of the co-registration variance of image pairs. This compromises the reliance on both the Rayleigh and the Rice distributions to derive uncertainties for the null and non-null displacements, respectively. When the directional co-registration variance σ_x^2 and σ_y^2 are not equal, the Euclidean distance l obeys a probability distribution that approaches that of a non-central Chi distribution for which an exact analytical estimation of the variance is not trivial.

Alternatively, the uncertainty of the displacement can be approached rigorously via error propagation similarly to Eq. (5) where Δx and Δy are the individual components of the displacement vector, corrected for any co-registration bias that exists. It follows that a rigorous estimate of the standard deviation associated with the measured displacement l for a vector on the glacier surface is given by

$$\sigma_l = \sqrt{\left(\frac{\Delta x}{l}\right)^2 \sigma_x^2 + \left(\frac{\Delta y}{l}\right)^2 \sigma_y^2}. \qquad (7)$$

In the general case and as illustrated in Fig. 4, the region of uncertainty surrounding the location of a feature identified at time t_2 is elliptical. Hence the standard deviation for each measurement is unique as it depends on the direction of the velocity vector.

3.5.2. *Validation of the theoretical approach*

Although rigorously obtained, Eq. (7) remains a first order approximation that may depart from the true uncertainty in some situations. This is especially true when the corrected displacement l becomes small relative to the error ellipse shown in Fig. 4. Therefore, a Monte Carlo experiment was employed to validate the error propagation approach.

$72{\times}10^7$ virtual displacements affected with a Gaussian noise were simulated for various nominal length, orientation, and flattening of the error ellipse (i.e., changing the ratio σ_x/σ_y). The size of the nominal displacements were chosen to range from 0.1 to 10 times the magnitude of the noise approximated by $\sqrt{\sigma_x^2 + \sigma_y^2}$. For each displacement-to-noise ratio (DNR) and orientation, the experimental uncertainty was calculated as the standard deviation of the set of discrepancies between the length of the noisy displacements and the nominal lengths across the corresponding Monte Carlo realizations. Modelled uncertainty was calculated based on Eq. (7), as well as using the Rayleigh distribution described above. The agreement was measured by the ratio between the modelled and experimental uncertainties and computed for each DNR and orientation.

Figure 5 illustrates the agreement between the modelled and experimental uncertainties as a function of the DNR. When the error propagation approach is used (i.e., Eq. 7) the distribution of the set of agreement ratios from the Monte Carlo realizations is depicted by means of the median and selected percentiles. In the case of the Rayleigh distribution, only the median of the corresponding set is shown for clarity purposes. Figure 5 demonstrates that Eq. (7) is valid as soon as the DNR approaches two. As the displacement reduces relative to the magnitude of the noise, Eq. (7) tends to overestimate the uncertainty by up to a factor 1.5, providing a more conservative estimate. Finally, Fig. 5 demonstrates the underestimation of the uncertainty when computed using the Rayleigh distribution as proposed by Necsoiu et al. (2009).

3.6. Assessing the co-registration of image pairs

The quality of the co-registration within image pairs was characterised in terms of bias (i.e., the solid shift of one image relative to the other, assumed to be constant across the subset area) and variance (i.e., the independent random displacement of each pixel). Co-registration assessment was implemented at a sub-pixel level, allowing variation of measured flow velocities between successive image pairs approaching or diminishing below the image pixel size to be detected.

Similarly to Necsoiu et al. (2009), co-registration was assessed by image matching. Displacements of more than 250 targets, known to be on stable ground (i.e., not on the glacier or on steep slopes) , and within the region immediately surrounding the Tasman Glacier. This sample size was large enough to provide statistically robust estimates of the co-registration bias vector (μ_x, μ_y) and directional variance (σ_x^2 and σ_y^2). Subtracting the bias vector from the displacements measured on the surface of the glacier yielded the corrected overall displacement l (see Fig. 4). The standard deviation of stable target displacements was then used to derive rigorous uncertainties for the glacier flow velocity measurements based on Eq. (7).

A unique confidence interval for each velocity measurement was calculated to generate a map of uncertainty associated with the velocity map for each image pair under consideration. In this study, maps of 90% confidence intervals were generated (i.e., $1.6 \times \sigma_l$) for the map of estimated velocities.

3.7. Change detection

Maps of velocity variation (i.e., flow acceleration and deceleration) were obtained by substracting the flow-fields associated with periods 2011–2010 and 2009–2010. The maps of uncertainty associated with each flow-field provided a threshold for inferring significant velocity changes on the Tasman Glacier. Confidence interval overlap testing was utilised in assessing the significance of mapped velocity change by applying a ternary classification whereby cells were classified as exhibiting significant acceleration, significant deceleration, or no significant velocity change, relative to determined thresholds. In this context, assessing the overlap of 90% confidence intervals corresponds to statistical testing at a higher significance level (e.g., 95%) (Cumming & Finch, 2005), further strengthening the inferences of change significance.

3.8. Comparison with the ground survey

Ultimately, the accuracy of the measurement obtained via image matching was assessed with respect to the displacements of markers installed on the surface of the glacier, surveyed as described in Section 2.3. A weighted regression was computed as described in York et al. (2004) to account for the uncertainties in both the reference and observed variables (i.e., GPS-derived and image-derived velocities have uncertainties derived from Eqs (1) and (7), respectively).

Table 2: Assessment of the co-registration of image pairs (in m).

Image pair	No. points	μ_x	μ_y	σ_x	σ_y
2009–2010	264	−0.91	−3.91	3.66	3.88
2010–2011	220	6.53	7.36	4.16	4.50

4. Results

4.1. Co-registration of the ASTER image pairs

Displacement measurements for 294 and 220 stable targets for the 2009–2010 and 2010–2011 image pairs respectively provided mean displacements in the x and y directions shown in Table 2. These displacements represent the average rigid translation between image pair constituents across the study area. While somewhat larger for the second of the two image pairs, this shift was less than one half of the native ASTER pixel size in all cases, thus demonstrating the quality co-registration obtained despite the independent ortho-rectification of each image.

Standard deviations of co-registration for the two image pairs were small (Table 2), less than one third of the native ASTER pixel size in all cases. This performance was comparable to the standard deviation of 3.5 m reported by Herman et al. (2011) based on the COSICorr software. The standard deviations for the 2010–2011 image pair were slightly larger than those for the 2009–2010 image pair, possibly due to worsening acquisition geometry, reflecting the larger look angle of the 2011 image. Standard deviations of co-registration were slightly larger in the y direction than the x direction for both image pairs, producing anisotropy in flow velocity uncertainties.

4.2. Band Performance

The set of 24 displacements observed on the ground and derived from image matching revealed contrasting performances of CIAS depending on the image channel used. ASTER band 3 exhibited the worst performance in this environment (Table 3), with the most mismatches, a poor regression and the largest RMSE. Although the enhancement with HP filter resulted in a slight increase of the success rate and a reduced RMSE, the regression did not improve. CIAS also returned lower correlation coefficients than with the original band 3, thus demonstrating no or limited benefit of this enhancement. The use of PAN and PC_1 channels yielded similar improvements across all measures with substantial benefit to the RMSE and success rate. Finally, band 1 achieved the best performance overall, with only a single mismatch and the smallest RMSE value. These results were consistent when computed for each image pair separately. The superior performance of ASTER band 1 over band 3 in this study was attributed to improved contrast associated with the spectral characteristics of debris covering the lower Tasman Glacier, as discussed in Section 5.4.

4.3. Validation of the image matching measurements

Velocities measured by CIAS agreed well with those measured *in situ* with GPS, as evidenced in Fig. 6. Eighty five per-

Table 3: ASTER bands and derived images tested against GPS measurements. Regression parameters correspond to a regression when y intercept is set to zero. The Root Mean Square Error (RMS) between the estimated and measured velocities is also reported, as well as the success rate (SR) of the image matching process.

Image	Regression	R^2 [%]	RMSE [m a^{-1}]	SR [%]	$\bar{\rho} \pm \sigma_\rho$
ASTER Band 1	$y = 0.98x$	85.2	16.5	95.8	0.73±0.03
ASTER Band 2	$y = 1.02x$	82.4	20.5	95.8	0.73±0.03
ASTER Band 3	$y = 1.22x$	25.5	60.1	79.2	0.71±0.04
Band 3 HP	$y = 1.10x$	16.1	54.6	83.3	0.63±0.03
PAN	$y = 1.15x$	73.0	33.1	91.7	0.77±0.03
PC_1	$y = 1.01x$	60.2	29.9	91.7	0.77±0.03

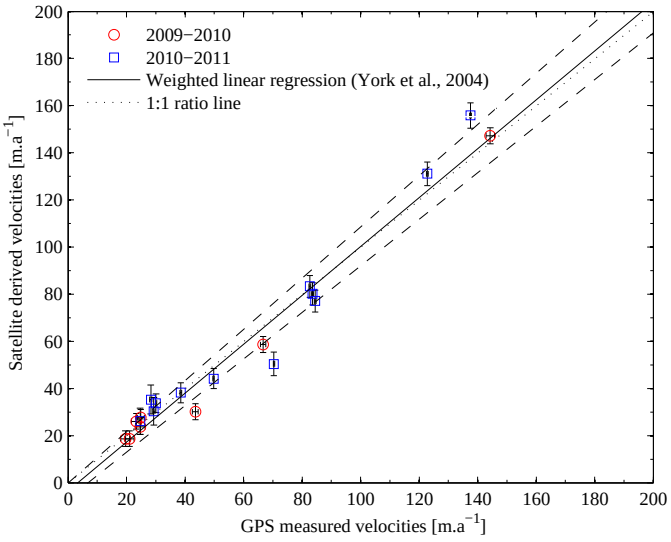

Figure 6: Regression plot of GPS measured vs. CIAS measured velocities for points surveyed by GPS in 2009. The weighted regression and 95% confidence interval are based on York et al. (2004).

cent of the measurements made by CIAS fell within the envelope of the weighted regression between CIAS and GPS measurements, thus providing good support for the methodology. With an $R^2 = 0.97$ (the confidence interval at the 95% confidence level is [0.92 – −0.99]) the correlation was significant and strong. Repeating the regression using the 2009–2010 and 2010–2011 data independently revealed that the agreement between CIAS- and GPS-derived velocities did not depart significantly from the 1:1 ratio line over either period, emphasising the reliability of the methodology.

4.4. Flow-field of the Tasman Glacier

Flow-fields derived for 2009–2010 and 2010–2011 display a similar structure. Flow velocities in excess of 300 m a^{-1} were measured on the upper part of the Tasman Glacier above the Hochstetter Confluence, decreasing markedly to minima less than 30 m a^{-1} in the confluence region (Fig. 7). Velocity decrease along the centre profile of the glacier was neither linear, nor uniform (Fig. 8). A decrease in velocity, between 10 and 12 km in Figure 8, was disrupted by an inflexion around 9-10 km along the flow profile. A rapid decrease in velocities was observed downstream of here toward the relatively slow moving area approximately 7.5 km along the flow profile (Figure 8), where flow velocities approached 20 m a^{-1} (Figure 7).

The influence of the Hochstetter Icefall on the lower glacier was obvious, with local velocity maxima approaching 300 m a^{-1} at the base of the icefall (see Figures 7 & 8). Flow velocities decrease rapidly down valley from the Hochstetter Icefall with a steadier decrease in velocity towards the tongue of the glacier. Velocities varied from around 150 m a^{-1} (up to 200 m a^{-1}) just beyond the foot of the icefall to less than 50 m a^{-1} towards Tasman Lake.

4.5. Flow velocity uncertainty and temporal change

In light of their magnitude relative to the pixel size of ASTER images and to the measured velocities, the uncertainties associated with velocity estimates were considered to be small. Confidence intervals (90%) varied between ±5.3 and ±5.6 m a^{-1} for the 2009–2010 flow-field and ±7.6 and ±8.2 m a^{-1} for the 2010–2011 flow-field. This corresponded to relative uncertainties of 34%, where flow velocity was measured as 37.9 m a^{-1}, to a minimum of 1.82%, where flow velocity was measured as 302.1 m a^{-1}.

Knowledge of uncertainties allowed the implementation of the change detection method described previously. Areas of significant velocity change across the surface of the Tasman Glacier between the 2009–2010 and 2010–2011 measurement periods were revealed. On the upper glacier, above the Hochstetter Confluence, regions of significant acceleration and deceleration up to ±50 m a^{-1} were observed. Below the Hochstetter Confluence, significant deceleration of about ±20 m a^{-1} was detected. No significant change was observed on the lower tongue of the glacier or in the terminus region.

5. Discussion

5.1. Flow field structure

Figures 7 and 8 illustrate the spatial structure of the flow-field of the Tasman Glacier as determined by image matching for the 2009–2010 and 2010–2011 periods.

The Rudolf Glacier appears to be a substantial tributary of the upper Tasman (i.e., upstream of the Hochstetter Icefall), but overall the flow-field in this area remains dominated by the flow from the main accumulation area of Tasman Glacier. Western tributaries north of the Hochstetter Confluence appear to exert little influence on the overall spatial structure of the flow-field. This suggests a relatively small mass flux through these tributary systems.

The flow-fields confirm that a discontinuity exists between the upper (Tasman) and lower (Hochstetter) glaciers, as suggested by Kääb (2002) and Quincey & Glasser (2009). The high velocity flow emerging from the base of the Hochstetter Icefall contrasts with the low velocities occurring a short distance up-glacier of the boundary between the Tasman and Hochstetter ice masses. Nevertheless, velocities derived from image matching remain significant over both years (see Fig. 8). Active flow

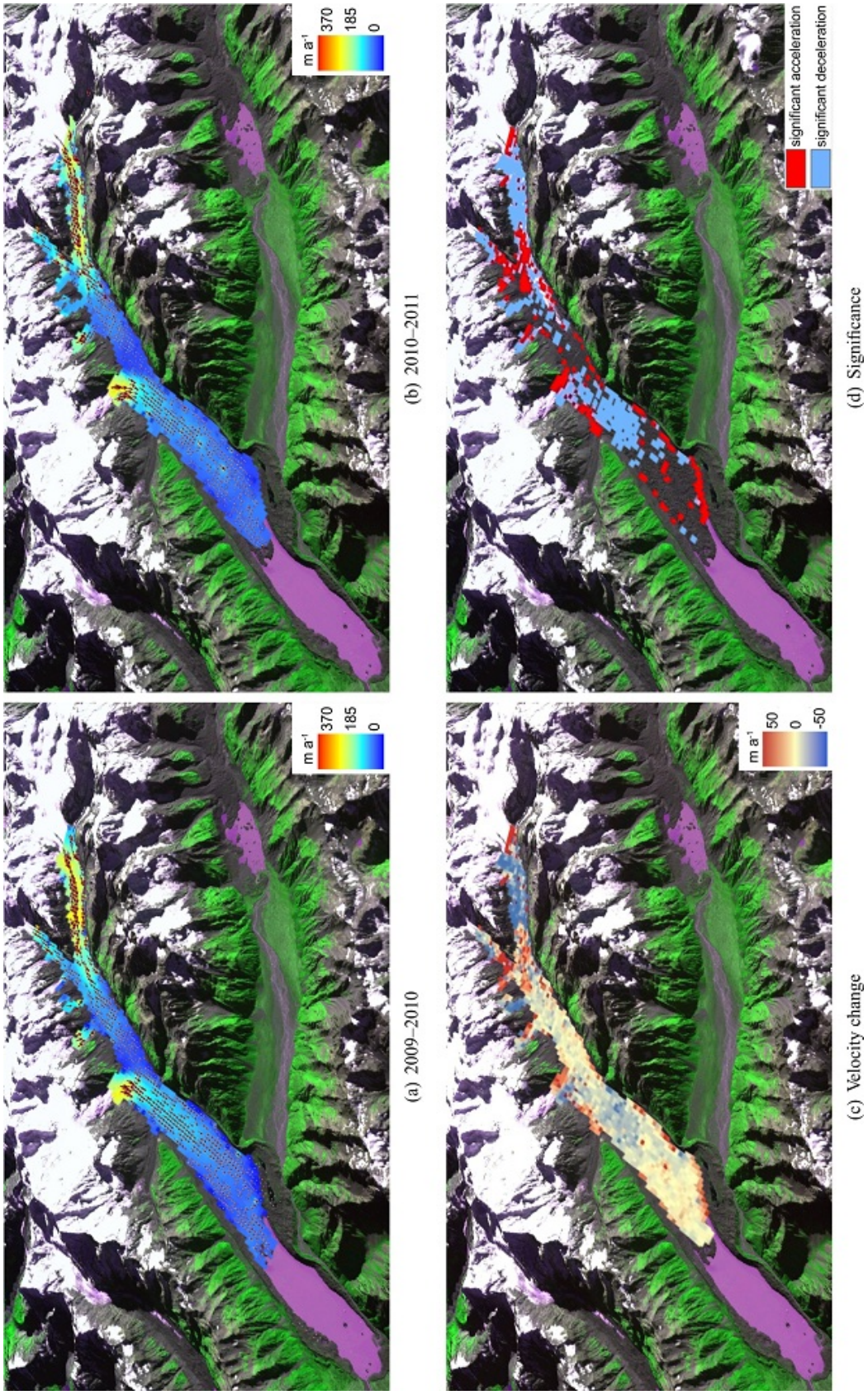

Figure 7: Maps of velocity for 2010 and 2011 (a) and (b); velocity change between 2010 and 2011 (c); and significance of the change (d), background image acquired April 9, 2010.

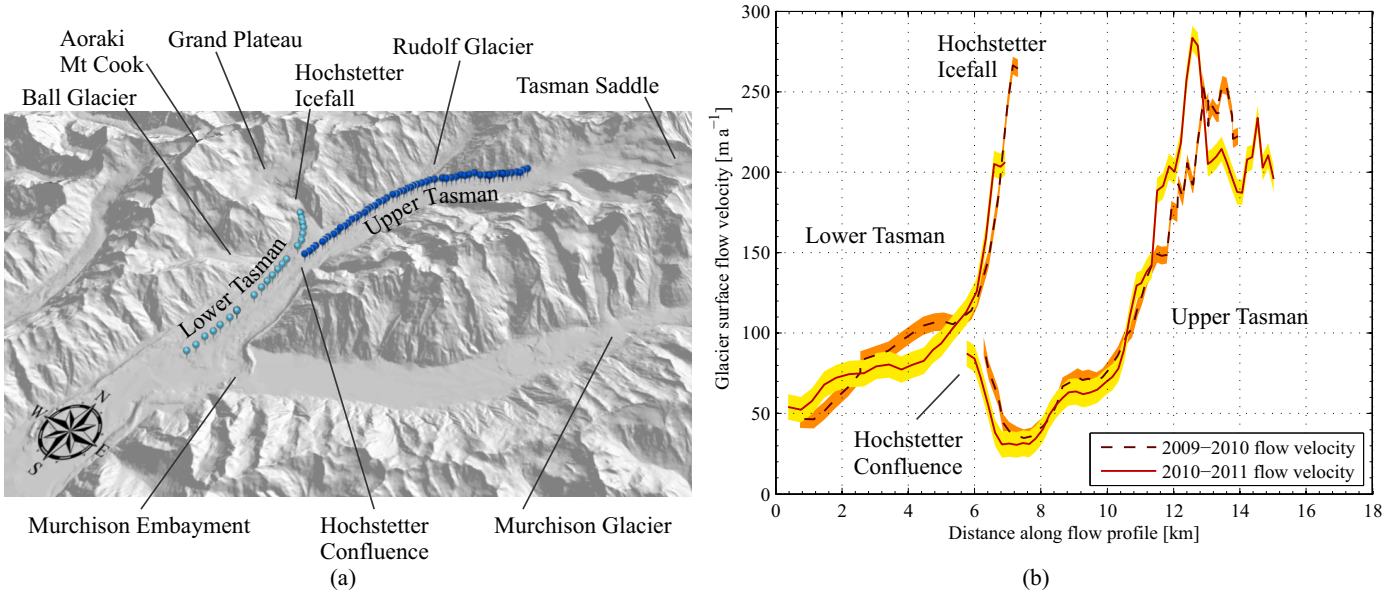

Figure 8: Longitudinal velocity profile for periods 2009–2010 and 2010–2011 extracted along the line shown above in the perspective projection. The envelope in (b) indicates the 90% confidence level on the velocity.

in this region was confirmed by the displacements measured on the ground (see Fig. 2). These observations indicate that the Tasman Glacier does not stagnate completely in this region, contrary to the conclusions of Quincey & Glasser (2009).

The Hochstetter Glacier is the major contributor to the flow of the lower section of the glacier. The Hochstetter Icefall drains the Grand Plateau (Figure 1), transferring a large mass of ice across a steep elevation gradient to the lower Tasman Glacier. Initially, the flow of ice from the Hochstetter Icefall is almost perpendicular to that of the upper Tasman Glacier. That this flow is diverted to the south, and divergent flow is not observed at the base of the icefall, indicates that the ice mass of the upper Tasman Glacier still exerts a significant influence over the dynamics of the lower glacier.

5.2. *Dynamic behaviour of Tasman Glacier*

The Tasman Glacier has been demonstrated as capable of exhibiting significantly dynamic behaviour on a yearly basis. Furthermore, this dynamic behaviour is not uniform across the glacier surface. Over the period 2009-2011, the surface flow has undergone a significant acceleration of about 25% at the confluence with the Rudolf Glacier. Conversely, most of the flow from the upper Tasman and that from the Hochestter Icefall towards the terminus slowed significantly, by up to the same amount, over this period (Fig. 8). In revealing the dynamic behaviour of the flow, these results shed new light on the conclusions of Quincey & Glasser (2009) and Herman et al. (2011) who could not detect significant change in velocity. Two methodological issues are suggested to have contributed to these conclusions.

First, both studies compared two periods of measurements that were greatly disconnected, specifically three and four years apart, respectively. Forming a conclusion about the overall dynamic of the flow from such a configuration requires an assumption that the flow velocity evolved in a monotonic way (i.e., that the flow was uniformly decelerating or accelerating throughout the period between the measurements). This assumption is, however, disputable given that glaciers are typically capable of expressing short-term variability in velocity (Sugiyama & Gudmundsson, 2004; Scherler & Strecker, 2012). The present study shows that the Tasman Glacier can speed up and slow down locally over the period of study. It is also likely that seasonal and even shorter-term variability may occur. Such variability compromises the ability to infer variations from the methodology used by Quincey & Glasser (2009) and Herman et al. (2011).

Second, by assuming that displacements measured via image matching obey a Rayleigh distribution, it has been shown that Herman et al. (2011) substantially underestimated uncertainties. Furthermore, reported errors for velocity in the range of the flow rate of Tasman Glacier largely exceeded the expected uncertainty. By considering larger but more reliable uncertainties, Herman et al. (2011) may have concluded that the short measurement period (16 days for each image pair) precluded the measurement of any displacement that could be qualified as significant. Significant change of velocity on the Tasman Glacier from one 16-day period to the next could therefore not be readily inferred in this context.

Finally, historical measurements at variable locations and time have led Kirkbride (1995) and Quincey & Glasser (2009) to conclude on an overall deceleration of the glacier. In contrast Kääb (2005b, pg. 132-133) concluded that an increase of surface velocity occurred over the period 2000-2002. Based on the result presented here, we believe that the dynamic of the flow of Tasman Glacier was not fully considered, and that not enough measurements, spatially and temporally, are yet available to reliably measure a significant trend. The results of this investigation lead us to conclude that regular measurements

based on connected measurement intervals and utilising the proposed uncertainty analysis would allow the flow dynamic to be adequately monitored. Such monitoring would facilitate an improved understanding of the processes governing the flow regime of the Tasman Glacier.

5.3. *Uncertainty associated with the flow field*

In light of their magnitude relative to the pixel size of ASTER images and to the measured velocities, the uncertainties associated with velocity estimates were considered to be small. Confidence intervals (90%) varied between ±5.3 and ±5.6 m a^{-1} for the 2009–2010 flow-field and ±7.6 and ±8.2 m a^{-1} for the 2010–2011 flow-field. This corresponded to relative uncertainties of 34%, where flow velocity was measured as 37.9 m a^{-1}, to a minimum of 1.82%, where flow velocity was measured as 302.1 m a^{-1}

5.3.1. *Deriving uncertainties in image matching algorithms*

The methodology to derive uncertainties and confidence intervals proposed in this study departs from the approach generally adopted by other studies. The co-registration bias between both images is determined, and accounted for by applying a correction to the raw velocity measurements. The co-registration variance is independently and selectively quantified in the x and y directions from the displacements of stable targets and rigorously propagated to the measured displacements. The potential anisotropy of uncertainties is readily accounted for, providing a more reliable signal of velocity change over time, from which the significance of temporal change may be confidently inferred. Given that valley glacier flow is inherently anisotropic, the ability to account for anisotropy within uncertainties is considered to be beneficial. Finally, the assessment of co-registration at a sub-pixel level allows confidence intervals to be substantially reduced (about a 10-fold decrease compared to Berthier et al. (2003) with a 2-fold reduction of pixel size).

5.3.2. *Accuracy assessment via independent ground information*

Unlike many previous studies relying on image matching, this study provided independent assessment of the methodology based on ground information. The good agreement with *in situ* data collected by GPS survey, over a time period nearly coincident with that between image acquisition, demonstrated the reliability and robustness of the image matching method. Although more ground data would always prove beneficial, its acquisition is complicated by the practicalities of conducting field work in remote and difficult terrain. Ground information also proved useful for assessment of the image matching technique, ensuring that the best performing band from ASTER imagery was used. This style of optimisation may benefit similar future studies.

5.3.3. *Topographic corrections and uncertainty*

Berthier et al. (2005) applied topographical corrections to measured displacements along the slope rather than reporting planimetric displacements. Slope effects have been ignored here, for two reasons. Firstly, the difficulties in constructing an accurate DEM of the surface of the Tasman Glacier for each period preclude such a task. Secondly, if DEMs were used, then it is believed that more uncertainty would be introduced than could be removed. For these reasons, DEM corrections of velocities measured on the Tasman Glacier are believed to be dubious and not necessary for assessing changes of velocity through time. Finally, the average surface gradient is relatively low across the ablation area of the Tasman Glacier. The major feature of the relief of the lower glacier is not the overall gradient, but the local surface morphology expressed by supraglacial features, which in turn provides many of the good targets for image matching.

5.4. *Band Performance*

Typically, ASTER band 3 has been used for image matching approaches to measuring displacements on glacier surfaces (Kääb, 2002, 2005b,a; Scherler et al., 2008; Quincey & Glasser, 2009; Herman et al., 2011). ASTER band 3 has generally been used in other similar studies because it is subject to less risk of saturation over ice and snow targets compared to bands 1 and 2, which is important for high latitude glaciers, or glaciers with a low surface debris supply and relatively stable surface morphology. Additionally, ASTER band 3 is commonly used to ensure consistency where bands 3N and B (which allows stereo-imaging) are used for the construction of DEMs used for image ortho-rectification. In the context of monitoring the displacement of sand dunes with COSI-Corr from a pair of ASTER and SPOT images, Necsoiu et al. (2009) questioned the performance of ASTER band 3 as it yielded higher level of noise and mismatches. Despite the lack of ground measurements and the reliance on a single image pair, this assessment was attributed to the spectral discrepancy with the SPOT panchromatic channel.

Based on two image pairs and 24 independent ground measurements, it has been shown here that ASTER band 1 outperformed band 3, or any of the other tested bands or combinations of bands for deriving velocities over the debris-covered Tasman Glacier with CIAS. This is attributed to the geological setting of the Tasman Glacier which consists of late Carboniferous to late Cretaceous age rocks, being characterised by the Torlesse composite terrane east of the Alpine Fault (Cox & Barrell, 2007). The rocks within this terrane are predominantly quartzofeldspathic indurated sedimentary rocks (referred to commonly as Greywacke), with localised metamorphism to semischist or schist (commonly known as Haast Schist). Within this terrane are a number of metamorphic zones, through which the mineral nature of constituent rocks changes significantly.

The Tasman Glacier is immediately surrounded by the pumpellyite-actinolite metamorphic zone (Cox & Barrell, 2007), providing a source for much of the surface debris. Data available from the ASTER spectral library, version 2.0 (Baldridge et al., 2009) indicates that the mineral actinolite has a peak reflectance in the range 0.5 to 0.6 μm, coincident with the spectral range of ASTER band 1 (Fig. 9). Thus, the local mineralogy lends itself to analysis within this spectral region, providing a reflectance level that should provide good contrast between illuminated and shadowed areas, without approaching

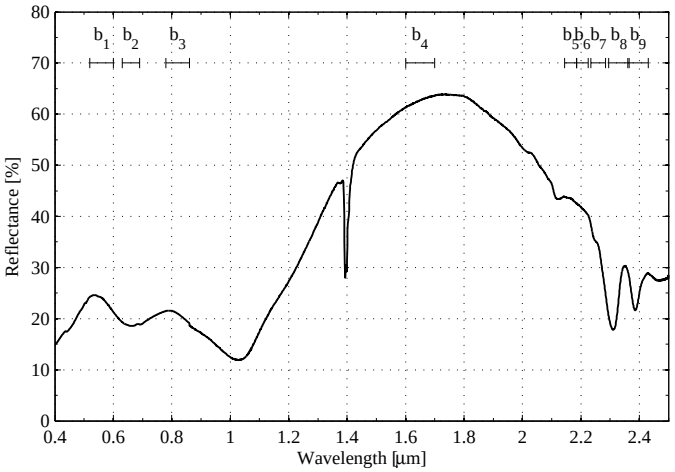

Figure 9: Spectral reflectance plot for mineral actinolite, obtained from the ASTER spectral library 2.0, http://speclib.jpl.nasa.gov (Baldridge et al., 2009); b1 to b9 indicate the location of ASTER spectral bands 1 to 9.

pixel saturation. The exposure of actinolite may be enhanced through the relatively fresh nature of supraglacial debris, much of which consists of rockfall deposits made up of broken and fractured rock fragments.

In light of contrasting band performance, we demonstrate that the selection of the band used in image matching algorithms has implications on the accuracy and reliability of the measurements. It is suggested that simple consideration of the spectral signature of target surface material may provide useful guidance for selecting a band that can support appropriate contrast, and should be incorporated as a fundamental methodological step in other similar studies.

6. Conclusions

Image matching using two successive ASTER image pairs has enabled a coherent field of flow measurements to be derived across the debris covered surface of the Tasman Glacier. Markers surveyed by GPS over two years were used to validate the image matching process. In addition, this *in situ* data was used to test the image matching performance of different spectral bands, demonstrating that ASTER band 1 outperformed ASTER band 3 for image matching over the debris covered Tasman Glacier. Local lithological influences provide a possible explanation for this result, with the debris exhibiting a peak reflectance in ASTER band 1, providing enhanced contrast to benefit the image matching process on this target surface. This finding also demonstrates that careful consideration should be given to the selection of an appropriate image channel for the target surface over which image matching is conducted.

Velocities measured by CIAS were found to be in close agreement with those measured by GPS and sub-pixel (relative to the native ASTER resolution of 15 m) level accuracy has been achieved. Uncertainties associated with velocity measurements presented here approach one third of the ASTER pixel size, or about 5 m. Such uncertainties have been determined through assessment of the quality of co-registration between the images for 2009, 2010, and 2011, and subsequent removal of co-registration bias. More importantly, this study proposes and demonstrates the validity of a new approach to estimate uncertainties based on the propagation of co-registration variance to measured displacements. This method can be applied to other contexts and locations when displacements have to be measured from repeated imagery. In estimating confidence intervals rigorously, better inferences and conclusions can be drawn about the dynamic of glaciers or other moving features.

Image matching results provided a flow-field for the Tasman Glacier over the period February 2009 to April 2011 that is in close agreement with previous studies in terms of the general spatial structure of the flow field. However, an improvement is offered in that the uncertainty analysis offered here allows the significance of temporal velocity changes to be easily and confidently assessed. Ultimately, it has been demonstrated that the Tasman Glacier experiences inter-annual variability within its surface flow-field over this period. A rigorous assessment of uncertainty is crucial to ensuring that such temporal signals can be reliably inferred.

Acknowledgments

This research is funded by the Department of Geography and School of Surveying, University of Otago, New Zealand. ASTER images were obtained with support from the Global Land Ice Measurement from Space (GLIMS). The authors also wish to thank Education New Zealand for its financial support.

References

Adams, J. B., & Gillespie, A. R. (2006). *Remote sensing of landscapes with spectral images: a physical modeling approach*. Cambridge, New York: Cambridge University Press, 362 pp.

Ahn, Y., & Howat, I. (2011). Efficient automated glacier surface velocity measurement from repeat images using multi-image/multichip and null exclusion feature tracking. *IEEE Transactions on Geoscience and Remote Sensing*, *49*(8), 2838–2846.

Allen, S., Gruber, S., & Owens, I. F. (2009). Exploring steep bedrock permafrost and its relationship with recent slope failures in the Southern Alps of New Zealand. *Permafrost and Periglacial Processes*, *20*(4), 345–256.

Anderton, P. W. (1975). Tasman Glacier 1971 - 73. hydrological research: Annual report 33. Tech. rep., Ministry of Works and Development, Wellington, New Zealand.

Baldridge, A., Hook, S., Grove, C., & Rivera, G. (2009). The aster spectral library version 2.0. *Remote Sensing of Environment*, *113*(4), 711–715.

Berthier, E., Raup, B., & Scambos, T. (2003). New velocity map and mass-balance estimate of Mertz Glacier, East Antarctica, derived from Landsat sequential imagery. *Jounral of Glaciology*, *49*(9), 503–511.

Berthier, E., Vadon, H., Baratoux, D., Arnaud, Y., Vincent, C., Fiegl, K., Rémy, F., & Legrésy, B. (2005). Surface motion of mountain glaciers derived from satellite optical imagery. *Remote Sensing of Environment*, *95*(1), 14–28.

Brodrick, T. (1891). Report on the Tasman Glacier. *Appendix to Journal of House of Representatives of New Zealand*, *Session II, Vol. 1. C1-A, Appendix 4*, 39–43.

Brodrick, T. N. (1894). Ice motion of Canterbury Glaciers. *New Zealand Alpine Journal*, *1*(6), 307–315.

Chinn, T. (2001). Distribution of the glacial water resources of New Zealand. *Journal of Hydrology (NZ)*, *40*(2), 139–187.

Columbus, J., Sirguey, P., & Tenzer, R. (2011). A free, fully assessed 15-m DEM for New Zealand. *Survey Quarterly*, *66*, 16–19.

Cox, S., & Barrell, D. (2007). *Geology of the Aoraki area*. Lower Hutt, New Zealand: Institute of Geological and Nuclear Sciences, GNS Science.

Cumming, G., & Finch, S. (2005). Inference by eye: Confidence intervals and how to read pictures of data. *American Psychologist*, *60*(2), 170–180.

Debella-Gilo, M., & Kääb, A. (2011). Sub-pixel precision image matching for measuring surface displacements on mass movements using normalized cross-correlation. *Remote Sensing of Environment*, *115*(1), 130–142.

Dodgson, N. A. (1992). Image Resampling. Tech. Rep. 261, University of Cambridge Computer Laboratory.

Gjermundsen, E., Mathieu, R., Kääb, A., Chinn, T., Fitzharris, B., & Hagen, J. (2011). Assessment of multispectral glacier mapping methods and derivation of glacier area changes, 1978-2002, in the central Southern Alps, New Zealand, from ASTER satellite data, field survey and existing inventory data. *Journal of Glaciology*, *57*(204), 667–683.

Heid, T., & Kääb, A. (2012). Evaluation of existing image matching methods for deriving glacier surface displacements globally from optical satellite imagery. *Remote Sensing of Environment*, *118*(0), 339–355.

Herman, F., Anderson, B., & Leprince, S. (2011). Mountain glacier velocity variation during a retreat-advance cycle quantified using sub-pixel analysis of ASTER images. *Journal of Glaciology*, *57*(202), 197–207.

Hubbard, B., & Glasser, N. F. (2005). *Field techniques in glaciology and glacial geomorphology*. Chichester, West Sussex, England: John Wiley & Sons, 412 pp.

Kääb, A. (2002). Monitoring high-mountain terrain deformation from repeated air- and spaceborne optical data: examples using digital aerial imagery and ASTER data. *ISPRS Journal of Photogrammetry & Remote Sensing*, *57*(1-2), 39–52.

Kääb, A. (2005a). Combination of SRTM3 and repeat ASTER data for deriving alpine glacier flow velocities in the Bhutan Himalaya. *Remote Sensing of Environment*, *94*(4), 463–474.

Kääb, A. (2005b). *Remote sensing of mountain glaciers and permafrost creep*,Zürich: Geographisches Institut der Universität Zürich, Schriftenreihe Physische Geographie, Glaziologie und Geomorphodynamik, 48, 266 pp.

Kääb, A., & Vollmer, M. (2000). Surface geometry, thickness changes and flow fields on creeping mountain permafrost: Automatic extraction by digital image analysis. *Permafrost and Periglacial Processes*, *11*(4), 315–326.

Kirkbride, M. P. (1993). The temporal significance of transitions from melting to calving termini at glaciers in the central Southern Alps of New Zealand. *The Holocene*, *3*(3), 232–240.

Kirkbride, M. P. (1995). Ice flow vectors on the debris mantled Tasman Glacier, 1957 - 1986. *Geografiska Annaler A*, *77*(3), 147–157.

Leprince, S., Barbot, S., Ayoub, F., & Avouac, J.-P. (2007). Automatic and precise orthorectification, coregistration, and subpixel correlation of satellite images, application to ground deformation measurements. *IEEE Transactions on Geoscience and Remote Sensing*, *45*(6), 1529–1558.

Lucchitta, B., & Ferguson, H. (1986). Antarctica: Measuring glacier velocity from satellite images. *Science*, *234*(4780), 1105–1108.

Moran, P. A. P. (1950). Notes on continuous stochastic phenomena. *Biometrika*, *37*(1-2), 17–23.

Necsoiu, M., Leprince, S., Hooper, D. M., Dinwiddie, C. L., McGinnis, R. N., & Walter, G. R. (2009). Monitoring migration rates of an active subarctic dune field using optical imagery. *Remote Sensing of Environment*, *113*(11), 2441–2447.

Paterson, W. S. B. (1994). *The Physics of Glaciers*, 3rd Edition. Oxford, UK: Butterworth Heinemann, 480 pp.

Quincey, D., & Glasser, N. (2009). Morphological and ice-dynamical changes on the Tasman Glacier, New Zealand, 1990-2007. *Global and Planetary Change*, *68*(3), 185–197.

Scambos, T., Dutkiewicz, M., Wilson, J., & Bindschadler, R. (1992). Application of image cross-correlation to the measurement of glacier velocity using satellite image data. *Remote Sensing of Environment*, *42*(3), 177–186.

Scherler, D., Leprince, S., & Strecker, M. R. (2008). Glacier-surface velocities in aline terrain from optical satellite imagery - Accuracy improvement and quality assessment. *Remote Sensing of Environment*, *112*(10), 3806–3819.

Scherler, D., & Strecker, M. R. (2012). Large surface velocity fluctuations of Biafo Glacier, central Karakoram, at high spatial and temporal resolution from optical satellite images. *Journal of Glaciology*, *58*(209), 569–580.

Strong, D. (2008). Patterns and processes of ice loss at Tasman Glacier : an evaluation using historic data sources and remotely sensed imagery. Master's thesis, University of Otago, Dunedin.

Sugiyama, S., & Gudmundsson, H. (2004). Short-term variations in glacier flow controlled by subglacial water pressure at Lauteraargletscher, Bernese Alps, Switzerland. *Journal of Glaciology*, *50*(170), 353–362.

Taylor, J. R. (1997). *An Introduction to Error Analysis: The study of uncertainties in physical measurements*, 2nd Edition. Sausalito, California: University Science Books, 327 pp.

Toutin, T. (2004). Review article: Geometric processing of remote sensing images: models, algorithms and methods. *International Journal of Remote Sensing*, *25*(10), 1893–1924.

York, D., Evensen, N. M., Martinez, M. L., & Delgado, J. D. B. (2004). Unified equations for the slope, intercept, and standard errors of the best straight line. *American Journal of Physics*, *72*(3), 367–375.